PCCP

Accepted Manuscript

ROYAL SOCIETY OF CHEMISTRY

www.rsc.org/pccp

On the importance of shear dissipative forces in coarse-grained dynamics of molecular liquids†

Sergei Izvekov* and Betsy M. Rice

Weapons and Materials Research Directorate, U.S. Army Research Laboratory, Aberdeen Proving Ground, Maryland 21005, USA

Abstract:

In this work we demonstrate from first principles that the shear frictions describing dissipative forces in the direction normal to the vector connecting the coarse-grained (CG) particles in dissipative particle dynamics (DPD) could be dominant for certain real molecular liquids at high-resolution coarse-graining. This is in contrast to previous works on bottom-up DPD modeling and indicates that such liquids cannot be simulated accurately using the conventional form of DPD which relies only on frictions in the radial direction. Specifically, we describe the development of fully bottom-up CG models for liquid hexahydro-1,3,5-trinitro-s-triazine (RDX) which are incorporated into the DPD method. Consistent with the microscopic foundation of DPD dynamics, the conservative part of the DPD models is obtained by the multi-scale coarse-graining (MS-CG) approach, which implements the pairwise decomposition of the atomistic potential of mean force (PMF) in CG coordinates. The radial and shear distant-dependent friction coefficients in a functional free form are derived systematically from microscopic velocity and force correlation data along system trajectories using a recently proposed approach [J. Chem. Phys. 140, 104104 (2014)]. The shear dissipative forces for the reported system appear to be dominant. We discuss the implications of dominant shear dissipation on dynamical and transport properties of CG liquids such as diffusion and viscosity as revealed by simulations of liquid RDX using the new MS-CG/DPD models.

1. Introduction

Computationally feasible modeling of liquids and soft-matter systems, such as polymers or weakly bound molecular aggregates, at the mesoscale requires a transition to discrete particle-like descriptions which could be obtained through two very distinct approaches, either top-down or bottom-up. Top-down modeling could be based on a discretization of the continuum hydrodynamic equations, which has demonstrated success at the mesoscale in going beyond simple Newtonian liquids, but still remains within an essentially macroscopic phenomenological framework.[1] A powerful alternative route is bottom-up particle-based coarse-graining in which groups of atoms are projected into a statistically equivalent ensemble of structureless coarse-grained (CG) particles interacting via mesoscopic force fields,[2-5] which upscale the underlying microscopic level interactions.

An important member in the family of the approaches for particle-based CG simulations of soft-matter systems is the dissipative particle dynamics (DPD) method, which initially was formulated by Hoogerbrugge and Koelman[6] in an effort to modify the Langevin dynamics heuristically to achieve momentum conservation, thereby leading to correct hydrodynamics. In this standard formulation of the DPD, the conservative and dissipative (friction and stochastic) forces are pairwise and *central* with amplitudes linearly decaying to zero. Español and Warren[7] derived fundamental equations relating the friction and stochastic force amplitudes ensuring compliance with the fluctuation-dissipation theorem (FDT) and hence existence of thermodynamic equilibrium in the DPD. Groot and Warren[8] pioneered efforts to derive the DPD models from detailed atomistic data. Subsequently, the DPD method has been further developed[7, 9-13] and demonstrated versatility for multi-scale simulations of complex systems including

polymers,[14] biological systems,[15-16] interfaces,[17-18] colloidal solutions,[19] and crystalline materials.[20]

Recently, within the Mori-Zwanzig projection operator method[21-24] it has been demonstrated[25-29] that the equilibrium dynamics of the center-of-mass of atomistic groups (e.g., clusters of molecules) representing the mesoparticles within a CG description is uniquely determined by the underlying microscopic dynamics. These have a form of the generalized Langevin equation (GLE). Within the pairwise and Markovian limits, which are always valid for systems interacting with nonlinear potentials at sufficiently aggressive coarse-graining,[30] the GLE dynamics acquire a classical Galilean invariant form of the DPD equations. The conservative component of the forces in the GLE-derived DPD equations are effective thermodynamic forces arising from the excess local free-energy and can be evaluated via a number of methods.[31-35] The free-energy origin of the conservative DPD/GLE forces translates into the ability of the effective dynamics, in which the non-conservative friction and stochastic forces are suppressed, to reproduce free-energy related equilibrium properties of the atomistic ensemble such as structure (e.g. RDFs) and thermodynamics.[36] Inclusion of non-conservative interactions has no effect on the system structure and thermodynamics; however, it restores the atomistic time correlations, thus ensuring correct transport properties.

A significant drawback of the standard DPD method lies in the empirical form for the non-conservative forces which include only radial frictions, while the microscopic GLE dynamics indicates the presence of non-central shear friction forces which act in a transverse-to-inter-particle connector direction. This deficiency of DPD has been first recognized by Español and collaborators.[37-39] Their extension of the DPD method incorporates two additional non-central shear components into the friction forces which are coupled to the stochastic forces by means of

the FDT. To restore angular momentum conservation violated due to presence of non-central shear forces, additional equations for torques and angular velocities of the particles were introduced.[40-41] The efforts to extend DPD method heuristically by including linearly decaying shear friction and stochastic forces were made by Kremer's group.[42] This work demonstrated very sensitive behavior of transport properties such as viscosity to the strength of dissipation in the transverse direction.

Although the DPD method has its roots in microscopic GLE dynamics, the parameterization of dissipative forces for DPD models has remained predominantly empirical over the course of time. More recently, new systematic approaches to extract the distance-dependent radial and shear dissipative forces directly from the microscopic data have been developed following the discovery of a link between the DPD and the first principles GLE interactions.[25, 29-30] Application of these approaches to various condensed-matter systems has revealed an interesting tendency of radial friction to be dominant if high-resolution coarse-graining (i.e., with fewer molecules per mesoparticle) is applied, while for large mesoparticles the radial and shear frictions become comparable. The latter observation is consistent with conclusions drawn from extensions of standard hydrodynamic DPD models.[41] In particular, for idealized Lennard-Jones fluid it was demonstrated by Lei *et al.*[43] that at all separations the radial friction dominates for clusters of smaller radii of gyration. For a single polymer chain coarse-grained into a dimer of blobs, a shear friction is negative while the radial friction remains positive for all separations.[44] The bottom-up blob picture of an elastic network representing models of crystalline systems has revealed a prevalence of the radial friction.[20] The dominance of the radial dissipation has also been observed for real molecular liquids and polymers, such as water,[45-46] nitromethane,[47] and star polymer melts,[28] if high-resolution coarse-graining is utilized.

Considering the aforementioned results on the relative importance of radial and shear dissipations, one might be tempted to conclude that a small size of mesoparticles provides sufficient grounds to simulate the DPD dissipation in the radial direction only. However, this conclusion has no *a priori* basis. In the present paper we present a counter-example of a real molecular liquid in which bottom-up coarse-graining into a one-site representation demonstrates the dominance of dissipation in the transverse direction. The molecular liquid is molten hexahydro-1,3,5-trinitro-*s*-triazine [RDX, the cyclic trimer of methylenenitramine $(CH_2NNO_2)_3$], a well-studied energetic molecular compound. RDX is in the crystalline state at ambient conditions and has an experimental melting point[48] of 478.6 K. We will report the development of the CG models of liquid RDX through several distinct steps. First, the pairwise effective interaction model is constructed from the force, velocity, and coordinate data sampled in all-atom empirical MD simulations by applying the multi-scale coarse-graining (MS-CG) method.[33, 49-51] Next, the same atomistic data are used to tabulate the non-conservative forces as distant-dependent complements to the MS-CG forces using an efficient bottom-up method recently introduced by us.[47] Friction coefficients calculated using the methods clearly exhibit the prevailing shear contribution. We discuss possible origins of such behavior and its impact on the dynamical and transport properties of the RDX via a comparison the properties from atomistic, effective (MS-CG), and MS-CG/DPD dynamics.

For the sake of convenience and clarity, in Sec. 2 we provide an overview of the bottom-up approaches for constructing numerically conservative and non-conservative DPD forces from the perspective of GLE dynamics. In Sec. 3, we apply these methodologies to coarse-grain the atomistic liquid RDX system and discuss the resulting models. Finally, in Sec. 4 we present concluding remarks.

2. Theoretical background

2.1 CG dynamics in the Markovian limit

Assuming an atomistic ensemble of M molecules is equally partitioned into N non-overlapping clusters of $N_{CG} = M/N$ molecules which represent mesoparticles in the CG description, equilibrium dynamics of center-of-masses (CoMs) of the clusters $\mathbf{R}^N = (\mathbf{R}_I, I = 1,\ldots,N)$ and their velocities $\mathbf{V}^N = (\mathbf{V}_I)$ remains Newtonian of the GLE form

$$M_{CG} d_t \mathbf{V}_I(t) = \mathbf{F}_I^{CG} + \mathbf{F}_I^D + \mathbf{F}_I^S , \tag{1}$$

$$d_t \mathbf{R}_I(t) = \mathbf{V}_I(t) \tag{2}$$

with M_{CG} denoting the total mass of the cluster. The first force term in eqn (1) is a conservative force

$$\mathbf{F}_I^{CG}(\mathbf{R}^N) = -\nabla_{\mathbf{R}_I} W^{PMF}(\mathbf{R}^N, V, T) , \tag{3}$$

where W^{PMF} is the all-particle CG potential of mean force (PMF), which is a thermodynamic potential.[25, 28-29] Within the standard DPD method the $\mathbf{F}_I^{CG}$ is a sum of linearly decaying two-particle central forces $f^{CG}(R)$

$$\mathbf{F}_I^{CG}(\mathbf{R}^N) \approx \sum_{J \neq I} f^{CG}(R_{IJ}) \mathbf{e}_{IJ} , \tag{4}$$

where $R_{IJ} = |\mathbf{R}_{IJ}|$, $\mathbf{e}_{IJ} = \mathbf{R}_{IJ}/R_{IJ}$, and $\mathbf{R}_{IJ} = \mathbf{R}_I - \mathbf{R}_J$. The strength of the interaction is adjusted to reproduce the generic quadratic equation of state giving rise to a target compressibility. The second term in eqn (1) is a dissipative force, which has the following form[28-29]

$$\mathbf{F}_I^D(t) = -\sum_{J \neq I} \int_0^t \left[\hat{\boldsymbol{\gamma}}_{IJ}\left(t-\tau, \mathbf{V}^N(\tau)\right) \bullet \mathbf{V}_{IJ}(\tau) - \frac{k_B T}{M^{CG}} \nabla_{\mathbf{V}_J}^T \bullet \hat{\boldsymbol{\gamma}}_{IJ}\left(t-\tau, \mathbf{V}^N(\tau)\right) \right] d\tau , \tag{5}$$

where $\mathbf{V}_{IJ}(t) = \mathbf{V}_I(t) - \mathbf{V}_J(t)$, and $\hat{\boldsymbol{\gamma}}_{IJ}(t)$ are the 3×3 friction tensors, which for a Markovian isotropic system approach a delta-function time dependence with no dependence on velocities:

$$\hat{\gamma}_{IJ}(t) = 2\begin{bmatrix} \gamma_{IJ}^{\parallel} & 0 \\ 0 & \gamma_{IJ}^{\perp} \end{bmatrix}\delta(t). \tag{6}$$

The $\gamma_{IJ}^{\parallel}, \gamma_{IJ}^{\perp}$ coefficients describe the friction forces in the radial (along vector $\mathbf{e}_{IJ}$) and transverse directions, respectively, in the Markovian limit

$$\mathbf{F}_I^D = -\sum_{J\neq I}\left(\gamma_{IJ}^{\parallel}\mathbf{V}_{IJ}^{\parallel} + \gamma_{IJ}^{\perp}\mathbf{V}_{IJ}^{\perp}\right) \tag{7}$$

while

$$\mathbf{V}_{IJ}^{\parallel} \equiv \left(\mathbf{V}_{IJ}\cdot\mathbf{e}_{IJ}\right)\mathbf{e}_{IJ};\ \mathbf{V}_{IJ}^{\perp} = \mathbf{V}_{IJ} - \mathbf{V}_{IJ}^{\parallel}. \tag{8}$$

The standard DPD method accounts for only radial frictions $\gamma_{IJ}^{\parallel}$. In contrast to the $\mathbf{F}_I^D$, the GLE stochastic force $\mathbf{F}_I^S$ [the third term in eqn (1)] is generally a non-pairwise complex thermodynamic average[29] which is difficult to evaluate directly from atomistic simulation.[28] Consequently, within the standard DPD framework the $\mathbf{F}_I^S(t)$ forces are modeled by a linear combination of standard Wiener (i.e., Gaussian white noise) random processes,[39] $f_{IJ}^{S.\alpha}(t)$, in the radial ($\alpha = \parallel$) and transverse ($\alpha = \perp$) directions. The tensors [eqn (6)] are related to the strength of the stochastic force through the FDT

$$\gamma_{IJ}^{\alpha} = \frac{1}{2k_BT}\left\langle\left(f_{IJ}^{S,\alpha}(0)\right)^2\right\rangle,\ \alpha = \parallel, \perp. \tag{9}$$

2.2 Conservative forces through the MS-CG method

The MS-CG method described elsewhere[33-34, 36, 50-57] is a first-principles approach for constructing the least-squares optimal pair-wise approximations [eqn (4)] to the effective force $\mathbf{F}_I^{CG}$ in eqn (3) by force-matching instantaneous atomistic CoM forces $\mathbf{F}_I^{CoM}$. In a practical

implementation of the MS-CG method, the $f^{CG}(R)$ functions in eqn (4) are cubic splines $f^{MSCG}(R)$ defined on a mesh $\{R_k\}$ up to a preselected cutoff distance R_{cut}^c:

$$f^{MSCG}(R) = A_k(R)f_k^{MSCG} + B_k(R)f_{k+1}^{MSCG} + C_k(R)\left[f_k^{MSCG}\right]'' + D_k(R)\left[f_{k+1}^{MSCG}\right]'', \; R_k < R < R_{k+1} \quad (10)$$

where $A_k = \left(R_{k+1} - R\right)/\Delta_k$, $B_k = 1 - A_k$, $C_k = \left(A_k^3 - A_k\right)\Delta_k^2/6$, $D_k = \left(B_k^3 - B_k\right)\Delta_k^2/6$, $\Delta_k = R_{k+1} - R_k$ is the *k*th bin size, and the f_k^{MSCG} and $\left[f_k^{MSCG}\right]''$ are values of the $f^{MSCG}(R)$ function and its second derivative at the kth node R_k of the mesh. The optimal parameter set $\left\{f_k^{MSCG}, \left[f_k^{MSCG}\right]''\right\} \equiv \Omega$ is determined from the following overdetermined system of linear equations,

$$\begin{cases} \sum_{J \neq I} f^{MSCG}(R_{Il,Jl}, \{R_k\}, \Omega)\mathbf{e}_{Il,Jl} = \mathbf{F}_{Il}^{CoM}; \quad I = 1, \ldots, N & (a) \\ \sum_{I<J} f^{MSCG}(R_{Il,Jl}, \{R_k\}, \Omega)R_{Il,Jl} = 3VP^{atm} - 2E_{kin,tr}^{atm} & (b) \\ f^{MSCG}(R_{cut}^c) = 0 \quad , \quad \left[f^{MSCG}\right]''(R_{cut}^c) = 0 & (c) \\ \left[f^{MSCG}\right]'_-(R_k) = \left[f^{MSCG}\right]'_+(R_k); \quad R_k \in \{R_k\} & (d) \\ l = 1, \ldots, L_{max}, \end{cases} \quad (11)$$

where Il labels the *I*th particle in the *l*th configuration along the trajectories and L_{max} is the total number of configurations sampled. The internal cluster free energy, which cannot be captured by the force-matching, can be recouped using an *ad hoc* pressure (or virial) constraint,[33] which is imposed by equation (*b*) in eqn (11), where P^{atm} and $E_{kin,tr}^{atm}$ are the respective instantaneous atomistic pressure and kinetic energy associated with the molecular translational (CoM) coordinates. The $f^{MSCG}(R,\Omega)$ and its second derivative are subject to zero boundary conditions at R_{cut}^c [constraints (*c*) in eqn (11)] and standard linear constraints requiring the f^{MSCG} to have

continuous first derivatives [equations (*d*)]. Equations (11) are solved using a block-averaging scheme.[33, 55] The potentials

$$w^{MSCG}(R_{IJ},\Omega)=\int_{R_{IJ}}^{R_{cut}^{c}} f^{MSCG}(R,\Omega)dR \tag{12}$$

implement a pairwise decomposition of the coarse-grained PMF $W^{PMF}(\mathbf{R}^N,V,T)\approx\sum_{I<J}w^{MSCG}(R_{IJ},\Omega)$ in eqn (3).

2.3 Dissipative and stochastic forces

Ref.[47] outlines the approach to derive $\gamma_{IJ}^{\parallel},\gamma_{IJ}^{\perp}$ frictions in a function-free form from microscopic force and velocity data. The approach exploits the orthogonality condition, - namely, the absence of statistical linear association between the stochastic forces and CG velocities at different time moments: $\left\langle \mathbf{F}_I^S(t)\mathbf{V}_J(0)\right\rangle\equiv 0,\ \ t>0$, for $\forall I,J$, which is a generic property of the GLE dynamics. The orthogonality condition allows the relation of the $\gamma_{IJ}^{\parallel},\gamma_{IJ}^{\perp}$ to two-body correlations, $c_{\Delta FV}^{\alpha}$, of residual force $\Delta\mathbf{F}_I=\mathbf{F}_I^{CoM}-\mathbf{F}_I^{CG}$ with velocity and three-body velocity-velocity correlations $\overline{c}_{VV}^{\alpha\beta}$ given by

$$\begin{aligned} &c_{\Delta FV}^{\alpha}\left(t,R_{IJ}\right)\equiv\left\langle\Delta\mathbf{F}_I(t)\cdot\mathbf{V}_J^{\alpha(IJ)}(0)\right\rangle,\\ &\overline{c}_{VV}^{\alpha\beta}\left(t,R_{IJ},R_{IL}\right)\equiv\left\langle\mathbf{V}_{IL}^{\alpha}(t)\cdot\mathbf{V}_J^{\beta(IJ)}(0)\right\rangle;\alpha,\beta\in\{\|,\perp\}\end{aligned} \tag{13}$$

where $\mathbf{V}_J^{\|(IJ)}(0)$, $\mathbf{V}_J^{\perp(IJ)}(0)$ are radial and transverse projections of the velocity vector $\mathbf{V}_J(0)$ with respect to vector $\mathbf{e}_{IJ}$ as described in eqn (8). For a translationally invariant system, the frictions become functions of only inter-particle distance as $\gamma_{IJ}^{\alpha}\equiv\gamma^{\alpha}\left(R_{IJ}\right)$, $\alpha\in\{\|,\perp\}$. They are uniquely determined on a preselected distance mesh $\left\{R_l,l=1,\ldots,N_{bin}\right\}$ up to the cutoff R_{cut}^{f}, where R_l is a center of the *l*th bin, by the correlation functions at a sufficiently large moment of time T_M from

$$\begin{cases} \sum_{\bar{l}=1}^{N_{bin}} \left[\bar{c}_{VV}^{\alpha\parallel}\left(T_M, R_l, R_{\bar{l}}\right)\gamma^{\parallel}\left(R_{\bar{l}}\right) + \bar{c}_{VV}^{\alpha\perp}\left(T_M, R_l, R_{\bar{l}}\right)\gamma^{\perp}\left(R_{\bar{l}}\right)\right] = -c_{\Delta FV}^{\alpha}(T_M, R_l) \\ l = 1,\ldots,N_{bin};\ \alpha \in \{\parallel,\perp\} \end{cases}, \quad (14)$$

which is a $2\times N_{bin}$ system of linear equations for $2\times N_{bin}$ unknowns $\left\{\gamma^{\parallel}\left(R_l\right), \gamma^{\perp}\left(R_l\right), l = 1,\ldots,N_{bin}\right\}$. Next, we can introduce the isotropic effective friction $\gamma^{eff}(R)$ as a solution of eqn (14) under the constraint $\gamma^{\parallel} = \gamma^{\perp} \equiv \gamma^{eff}$. The respective equations form an *overdetermined* system of $2\times N_{bin}$ equations for N_{bin} unknowns $\gamma^{eff}(R_l)$

$$\left\{ \sum_{\bar{l}=1}^{N_{bin}} \bar{c}_{VV}^{\alpha\parallel}\left(T_M, R_l, R_{\bar{l}}\right)\gamma^{eff}\left(R_{\bar{l}}\right) = -c_{\Delta FV}^{\alpha}(T_M, R_l),\ l = 1,\ldots,N_{bin};\ \alpha \in \{\parallel,\perp\} \right. . \quad (15)$$

The systems of equations (14) and (15) can be efficiently solved in a least-squares sense using standard techniques. Once the $\gamma^{\parallel}, \gamma^{\perp}$ or γ^{eff} are determined, the strength of the Wiener stochastic force can be determined via the FDT relation in eqn (9).

The many-body contributions to the conservative force may effectively increase the strength of the frictions derived in accordance with eqn (14), (15). Observing that an average number of particles at a distance R from the Ith particle is $d\left\langle N(R)\right\rangle = N/V g_{CoM}(R) 4\pi R^2\, dR$, where $g_{CoM}(R)$ is the molecular CoM RDF, from eqn (1), (5), (6) we immediately obtain

$$\left\langle \Delta\mathbf{F}_I^2 \right\rangle = \frac{4\pi k_B T N}{V} \int_0^{\infty} \left(\frac{1}{M_{CG}} \left[\gamma^{\parallel}(R)^2 + 2\gamma^{\perp}(R)^2 \right] + 2\left[\gamma^{\parallel}(R) + 2\gamma^{\perp}(R) \right] \right) g_{CoM}(R) R^2 dR\,. \quad (16)$$

On the other hand, the $\left\langle \Delta\mathbf{F}_I^2 \right\rangle$ is the absolute error of the force-matching eqn (11). Since the exact effective force in eqn (3) minimizes the $\left\langle \Delta\mathbf{F}_I^2 \right\rangle$, any missed (e.g., many-body) contribution into the residual force $\Delta\mathbf{F}_I$ effectively increases the $\left\langle \Delta\mathbf{F}_I^2 \right\rangle$. In accordance with eqn (16) this always leads to stronger friction.[43-44]

3. Results

3.1 Microscopic reference system

The RDX molecule (Fig. 1a and Fig. S1, ESI) is a six-membered ring of carbon and nitrogen atoms, with three nitro groups positioned in either an axial (*a*, normal) or equatorial (*e*, parallel) orientation relative to the central ring, and can assume a variety of conformers. Within high-resolution coarse-graining (by DPD standards), the RDX molecule is mapped onto a single spherically symmetric site associated with the location of the molecular CoM location as depicted in Fig. 1a. Atomistic simulations of the RDX system were performed using the all-atom flexible force field developed by Smith and Bharadwaj (SB model).[58-59] The SB model accurately predicts many physical properties of various phases of RDX, including the liquid state.[51, 60-61] The structure of the isolated RDX molecule at $T = 0$ K optimized using the SB model is shown in Fig. 1a, and has the *Caee* conformation (*C* stands for a "Chair" conformer of central ring).

The microscopic system was modeled by a supercell of liquid RDX under constant *NVT* conditions at $T = 550\,\mathrm{K}$ (Fig. 1b) and density of 1564.4 kg/m3; periodic boundary conditions were imposed in all three directions. The coordinates, velocities, and virials quantities were sampled at 2 ps intervals for 30 ns and are herein referred to as "set-long". Due to a faster convergence, the $c^{\alpha}_{\Delta FV}$ and $\overline{c}^{\alpha\beta}_{VV}$ in eqn (13) were calculated from trajectories having a duration of 15 ps and sampled at 0.001 ps time interval (referred to as "set-short"). The atomistic trajectories were coarse-grained by mapping the molecules into the respective instantaneous CoM locations, and the atomistic velocities and forces into the respective CoM quantities.

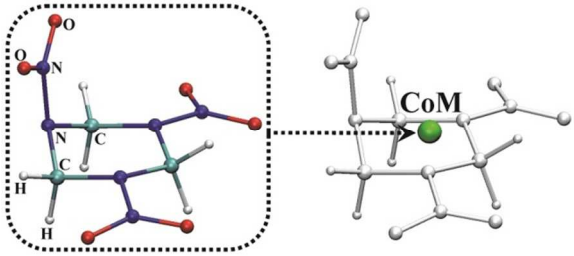

(a)

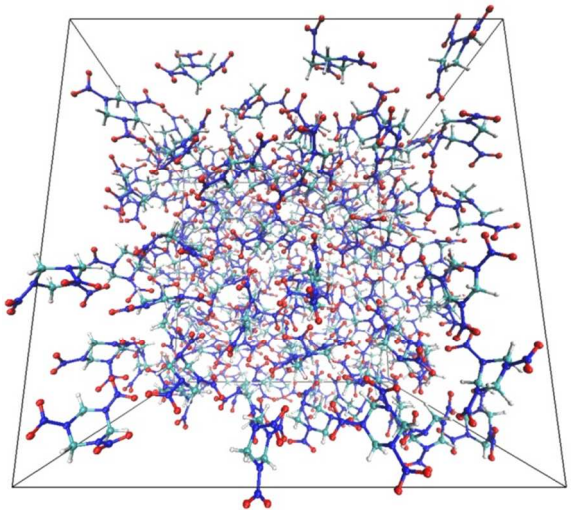

(b)

Fig. 1 Panel (a): Isolated RDX molecule in the *Caee* conformation at $T = 0$ K for the SB model and its coarse-graining into the one-site representation. Panel (b): Simulation cell of atomistic liquid RDX.

3.2 Conservative forces in liquid RDX

The MS-CG pairwise approximation to the conservative force, $f^{MSCG}(R)$, eqn (4), (10), was determined by solving eqn (11) in the same way as in ref.[51] The relative standard deviation, $\bar{\sigma} \equiv \left(\sigma^2[\mathbf{F}^{CoM}]\right)^{1/2} \Big/ \left(\sum_I \left|\mathbf{F}_I^{CoM}\right|^2\right)^{1/2}$, where σ^2 is variance, of the force matching is $\bar{\sigma} = 0.94$ reflecting both the importance of many-body contributions in the conservative forces and the strength of the non-conservative forces [eq. (16)]. The $f^{MSCG}(R)$ force was assumed to have an

exponential form for unsampled short distances $R < R_{core}$ as described in ref.[47] The conservative force (referred to as the MS-CG model, Fig. 2) was then validated in CG simulations of liquid RDX at the reference atomistic conditions ($T = 550$ K and $P = 0$). The pressure constraints made the $f^{MSCG}(R)$ significantly more attractive (by ~10.5 kJ/mol) resulting in an equilibrium density within 1.4% of the atomistic value. The conservative force derived without pressure constraints (dotted lines in Fig. 2) resulted in a pressure in excess of 2 MPa under the reference *NVT* conditions. The MS-CG model reproduces accurately the liquid pairwise structure (molecular RDF) as demonstrated in Fig. S2.

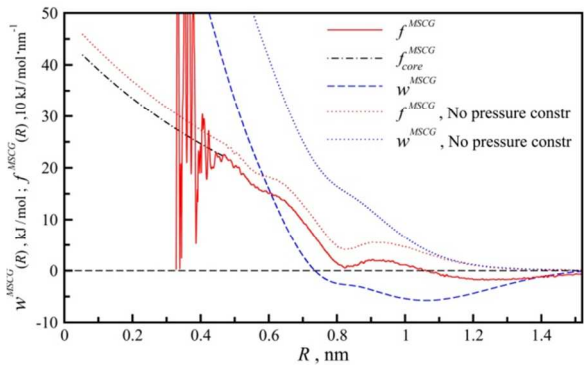

Fig. 2 Spline profile for the $f^{MSCG}(R)$ force (red solid) for the one-site liquid RDX obtained using the force-matching procedure [eqn (11)] and corresponding potential $w^{MSCG}(R)$ [eqn (12)] (blue dashed). The exponential core of the $f^{MSCG}(R)$ is shown in a black dot-dashed line. The dotted lines display the $f^{MSCG}(R)$ (red) and $w^{MSCG}(R)$ (blue) derived without the pressure constraints (b) in eqn (11).

3.3 DPD non-conservative forces in liquid RDX

The "set-short" trajectories were utilized to tabulate $\gamma^{\parallel}(R), \gamma^{\perp}(R)$ via solving eqn (14) and $\gamma^{eff}(R)$ via solving eqn (15). The time T_M in eqn (14), (15) should be large enough that the

transition to the Markovian form of the memory function in eqn (5) is justified.[47] The discussion below is illustrated in Fig. S3. Following ref,[47] The T_M was selected from the period of time $t > T_{c,max}$, where $T_{c,max}$ (0.61 ps) corresponds to the time at which the ratio $-c_{\Delta FV}(t)/c_{VV}(t) \cong \gamma = 930.7$ kJ/mol·ps/nm^2 (1 kJ/mol·ps/nm^2 $= 1.660539\times10^{-15}$ kg/s), where $c_{VV}(t) \equiv \langle \mathbf{V}_I(t)\cdot\mathbf{V}_I(0)\rangle$, is approximately independent of t (dashed line in Fig. S3). For the chosen R_{cut}^f, the correlations $c_{\Delta FV}^{\alpha}$, $c_{VV}^{\alpha\beta}$ were obtained in the form of histograms, i.e., $\{c_{VV}^{\alpha\beta}(t,R_l), l = 1,\ldots,N_{bin}\}$ employing the same estimators as described in ref.[47] The frictions were then computed as similar histograms which, for the production DPD simulations, were smoothed out with a Gaussian filter[47] (the details are given in the ESI).

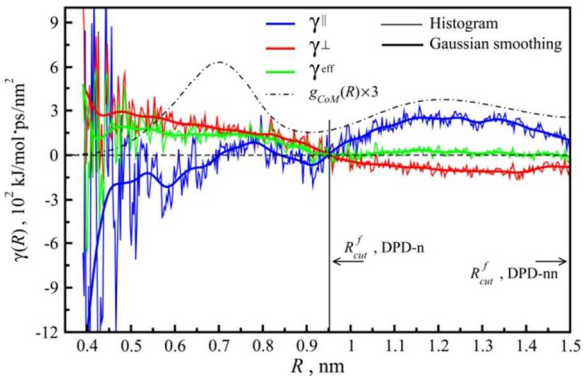

Fig. 3 Histogram data (thin noisy) and its Gaussian filter smoothing [eqn (S1), (S2) in the ESI] (thick) of friction coefficients: $\gamma^{\parallel}(R)$, $\gamma^{\perp}(R)$, $\gamma^{eff}(R)$ for the one-site MS-CG RDX liquid. The scaled CoM RDF is shown by the dot-dashed line. The vertical lines and arrows show the choice of distance cutoff to frictions, R_{cut}^f, for the respective MS-CG/DPD model.

The calculated $\gamma^{\parallel}(R)$, $\gamma^{\perp}(R)$, and $\gamma^{eff}(R)$ are plotted in Fig. 3. The $\gamma^{\parallel}(R)$, $\gamma^{\perp}(R)$ for the liquid RDX are very different from those obtained for the one-site representation of liquid nitromethane (NM).[47] The NM molecule is smaller and of higher symmetry, and in particular has a higher aspect ratio compared to RDX. In liquid NM, the radial dissipation appears to be dominant between the molecules from the first coordination shell, i.e., at $R < R\left[g^{1}_{\min}\right]$, where $R\left[g^{i}_{\min(\max)}\right]$ denotes the location of the *i*th minimum(maximum) in the molecular CoM RDF $g_{CoM}(R)$ (see Fig. S2 and Fig. 3). This observation is similar to reported results from bottom-up DPD models of molecular liquids and polymers at high resolution coarse-graining. In contrast, a major contribution to the friction between nearest-neighbors in liquid RDX comes from the shear component. In fact, the RDX $\gamma^{\parallel}(R)$ in the first coordination shell is negative except for a small (0.05 nm wide) region. The $\gamma^{\parallel}(R)$, $\gamma^{\perp}(R)$ in the second coordination shell, $R\left[g^{1}_{\min}\right] < R < R\left[g^{2}_{\min}\right]$, behave similarly to that of liquid NM as well as other liquid systems reported in the literature: $\gamma^{\parallel}(R)$ is positive and its shape resembles the $g_{CoM}(R)$, while the $\gamma^{\perp}(R)$ is negative. Meanwhile, the effective friction $\gamma^{eff}(R)$ is positive everywhere. The signs of the $\gamma^{\parallel}(R)$ and $\gamma^{\perp}(R)$ are merely reflections of the direction of energy flow between the CG and irrelevant coordinates when the dissipative particle either departs from or orbits about a reference particle.[28] The negative dissipation $\gamma^{\parallel,\perp}(R)$ at certain separations is indicative of a short-ranged molecular translational and angular ordering which reduces the system local entropy at these separations. This in turn increases the probability of energy release into the CG subsystem. Possible related explanations for the negative $\gamma^{\parallel}(R)$ in the first coordination shell $R < R\left[g^{1}_{\min}\right]$

include strong radial depletion effects which tend to pull the molecules to the most probable interparticle separation: $R\left[g^1_{\max}\right]$. Likewise, the $\gamma^{\perp}(R)>0$ at $R<R\left[g^1_{\min}\right]$ indicates the absence of significant angular ordering in the first coordination shell. The situation is reversed in the second coordination shell.

In DPD simulations with Wiener random forces to fulfill the FDT in eqn (9), the $\gamma^{\parallel}(R)$, $\gamma^{\perp}(R)$ frictions must be set to zero if they are negative. This may contribute to disagreement with atomistic dynamics where both negative and positive rates of dissipation are permitted. These considerations are not relevant for a system with all frictions described using the strictly positive $\gamma^{eff}(R)$. Therefore, to better elucidate the importance of dissipation in the radial and transverse directions we consider three MS-CG/DPD models. The first two models, referred to as the DPD-n and DPD-nn models, are those in which the $\gamma^{\parallel}(R)$ and $\gamma^{\perp}(R)$ frictions are set explicitly. The main difference between the DPD-n and -nn models is that in addition to friction between nearest (-n) neighbors, the DPD-nn model has a non-vanishing radial friction between molecules from the second coordination shell [i.e., between nearest-next (-nn) neighbors]. Consequently, the models differ by the cutoff distance R^f_{cut} applied to the frictions (see Table 1 and Fig. 3). For the DPD-n, the R^f_{cut} is close to $R\left[g^1_{\min}\right]$ and at which $\gamma^{\perp}(R^f_{cut})=0$. For the DPD-nn, $R^f_{cut}=R^c_{cut}$, which is close to $R\left[g^2_{\min}\right]$. In the third model, denoted DPD-eff, the $\gamma^{\parallel}(R)$ and $\gamma^{\perp}(R)$ are replaced with the $\gamma^{eff}(R)$ and the cutoff is set to $R^f_{cut}=R^c_{cut}$. The overall strength of frictions for different models can be conveniently compared in terms of their integral (volume-averaged) values

$$\overline{\gamma}^{\parallel,\perp} = \frac{4\pi N}{V} \int_0^{R_{cut}^f} \gamma^{\parallel,\perp}(R) g_{CoM}(R) R^2 dR \,. \quad (17)$$

Table 1 shows that the DPD-nn exhibits the strongest integral dissipation, followed by the DPD-eff and then DPD-n models. For the DPD-nn and –n model, this difference arises due to the difference in the radial dissipation, since these models by construction have the same $\gamma^{\perp}(R)$ frictions. Furthermore, though the DPD-eff has a smaller $\gamma^{\perp}(R)$ in the first coordination shell, it has nearly the same values of $\overline{\gamma}^{\perp}$ as that of the other two models due to a positively defined $\gamma^{\perp}(R)$ in the second coordination shell. As discussed below, this feature might explain similarities in the viscous properties of the DPD models.

model	R_{cut}^f / R_{cut}^c	$\overline{\gamma}^{\parallel} / \overline{\gamma}^{eff}$	$\overline{\gamma}^{\perp} / \overline{\gamma}^{eff}$	D_{diff}	τ_s, τ_{MSD}, τ_l	η
Atm	-"-	-"-	-"-	0.14	6.1, 6.2, 202	11.8 (1.5)
MS-CG	0.0	-"-	-"-	5.74	4.0, 0.7, 40	0.6(0.03)
MS-CG/DPD-n	0.620	0.143	1.004	0.76	5.8, 1.9, 96	3.2(0.2)
MS-CG/DPD-nn	1.0	4.132	1.004	0.28	6.4, 4.9, 140	3.1(0.3)
MS-CG/DPD-eff	1.0	1.0	1.0	0.61	5.3, 2.4, 105	3.4(0.3)

Table 1 For MS-CG/DPD models, ratios R_{cut}^f / R_{cut}^c of cutoffs distances for friction and conservative forces are shown, as well as ratios $\overline{\gamma}^{\parallel} / \overline{\gamma}^{eff}$, $\overline{\gamma}^{\perp} / \overline{\gamma}^{eff}$ of volume averaged friction coefficients from eqn (17) using atomistic g_{CoM}. The rest of the Table compares transport properties of liquid RDX: diffusion coefficients D_{diff} (10^{-9} m^2/s); residence times (ps): short time τ_s, short time τ_{MSD} as determined from MSD [eqn (23), Fig. S4],

and long time τ_l; shear viscosity η coefficients (10^{-3} Pa·s) with standard deviation shown in brackets, from different models.

3.4 Dynamic and transport properties

The transport coefficients, such as self-diffusion D_{diff} and shear viscosity η, are determined by time autocorrelations of certain phase variables through the Green-Kubo (GK) relations. For self-diffusion, the GK relation is

$$D_{diff} = \frac{1}{3}\int_0^\infty c_{VV}(t)dt \tag{18}$$

and for viscosity

$$\eta = \lim_{t\to\infty}\eta(t) \equiv \lim_{t\to\infty}\frac{V}{k_B T}\int_0^t c_{\sigma\sigma}^{xy}(t')dt', \tag{19}$$

where $c_{\sigma\sigma}^{xy}(t) = \left\langle \sigma_{xy}(t)\sigma_{xy}(0)\right\rangle$ is the autocorrelation function of the off-diagonal components of the stress tensor $\hat{\boldsymbol{\sigma}}$. The power spectrum of $c_{VV}(t)$,

$$\tilde{c}_{VV}(\lambda) = \frac{\int_0^\infty c_{VV}(t)\cos(2\pi\lambda t)dt}{c_{VV}(0)}, \tag{20}$$

describes (within the harmonic approximation) the vibrational density of states (VDOS) on which many thermodynamic properties depend. In general, the D_{diff} can be calculated from the slope of the molecular mean-squared displacement (MSD) $\overline{\Delta\mathbf{R}^2}(t) \equiv \left\langle \left|\mathbf{R}_I(t) - \mathbf{R}_I(0)\right|^2 \right\rangle$ via the Einstein relationship. Useful insight into the dynamics in the RDX melt is provided by the survival time correlation function, $C^S(t)$, which defines the probability that a molecule remains

in the first coordination shell during the time period from 0 to t. For a simple liquid, the $C^S(t)$ can be defined as

$$C^S(t) = \frac{1}{N}\sum_{I=1}^{N} C_I^S(t) = \frac{1}{N}\sum_{I=1}^{N} \frac{\left\langle \sum_{J\neq I} \vartheta_{IJ}(t)\vartheta_{IJ}(0) \right\rangle}{\left\langle \sum_{J\neq I} \vartheta_{IJ}(0)\vartheta_{IJ}(0) \right\rangle}, \quad (21)$$

where $C_I^S(t)$ is the survival time correlation function for the first coordination shell of the *I*th molecule. Adapting the definition which is commonly used for solutions,[62] the $C_I^S(t)$ in eqn (21) is introduced as autocorrelations of $\vartheta_{IJ}(t)$, where the $\vartheta_{IJ}(t)$ is the Heaviside step function, and is equal to unity if molecule *J* remains in the first coordination shell of molecule *I* more than the delay time t_d (set to 1 ps) during the $t + 2t_d$ period of time and is zero otherwise. The first peak in the $g_{CoM}(R)$ can be interpreted as the labeled molecule immobilized within a cage formed by the nearest neighbors for the residence time τ, which can also be viewed as the time needed for the molecule to escape from the cage. The residence times quantify the relaxation of the local structure and along with the MSD and velocity autocorrelations may help to provide further insight into the quasi-caged dynamics which impact the transport properties. Such dynamics typically spans multiple time scales and thus is better described by invoking many residence time constants. For instance, in the two-scale picture of caged dynamics, decay constants for the short and long residence times, (τ_s and τ_l, respectively), can be determined by fitting the $C^S(t)$ with a double exponent

$$C^S(t) \approx A_s \exp(-t/\tau_s) + A_l \exp(-t/\tau_l). \quad (22)$$

Noting that the mean-squared change of intermolecular separation $\overline{\Delta\mathbf{R}_{IJ}^2}(t) \equiv \left\langle \left| \mathbf{R}_{IJ}(t) - \mathbf{R}_{IJ}(0) \right|^2 \right\rangle$ is related to the MSD $\overline{\Delta\mathbf{R}^2}(t)$ as $\overline{\Delta\mathbf{R}_{IJ}^2}(t) = 2\overline{\Delta\mathbf{R}^2}(t)$, the residence time τ_{MSD} can be also estimated from

$$\frac{1}{2}\left(R[g^1_{\min}] - R[g^1_{\max}] \right)^2 = \overline{\Delta\mathbf{R}^2}(\tau_{MSD}) \tag{23}$$

(as illustrated in Fig. S4). The τ_{MSD} from eqn (23) represents the average time for a molecule to diffuse from the most probable location within the first coordination shell, $R[g^1_{\max}]$, to the edge of the shell, $R[g^1_{\min}]$, and might differ from the τ_s if the diffusive regime is not established on the short time scale.

The diffusion D_{diff} and residence time constants τ_s, τ_l, τ_{MSD} are summarized in Table 1. The survival time correlation functions $C^S(t)$ are compared in Fig. 4. The MS-CG/DPD models routinely overestimate the diffusion rate. The smallest D_{diff} is twice the atomistic value and is given by the DPD-nn model, which accounts for the $\gamma^{\parallel}(R)$ in the first two coordination shells, followed by the DPD-eff and then the DPD-n models. This naturally correlates with the strength of the integral radial frictions $\bar{\gamma}^{\parallel}$ (Table 1). Although the DPD-nn model best describes self-diffusion properties, it performs poorly compared to the DPD-n and DPD-eff models, both limiting the radial an shear dissipative interactions to the first coordination shell, in how well the short-time (~ 2 ps) dynamics is captured. The short-time dynamics spans the ballistic regime [$\overline{\Delta\mathbf{R}^2}(t) \propto t^2$] and transient to the diffusive regime [$\overline{\Delta\mathbf{R}^2}(t) \propto t$] periods [see insert to Fig. 4S]. The dynamics at these scales is a signature of caged dynamics and thus provides a quantitative tool to gain insight into the mesoscopic origin of model performance in simulating transport

properties. It appears that the short-time behavior is best modeled by the DPD-n model. This can be inferred by comparing the τ_s constants shown in Table 1 and the $C^S(t)$, $\overline{\Delta \mathbf{R}^2}(t)$ curves shown in the inserts in Fig. 4 and Fig. S4 as well the liquid $c_{VV}(t)$ shown in Fig. S5a in the ESI. In particular, for the DPD-n model both the short-time $C^S(t)$ correlations and the τ_s constant closely follow the atomistic counterparts. (The discrepancy between τ_{MSD} and τ_s for faster models can be explained by the failure of eqn (23) if the diffusive regime is not reached on a scale of τ_{MSD}). In fact the DPD-nn,-eff models exhibit a stronger dissipation and achieve a slower diffusion at the cost of significant overdamping the short-time dynamics [clearly seen from the shape of $C^S(t)$ and $c_{VV}(t)$ curves at small times in Fig. 4 and Fig. S5]. At intermediate times (up to 30 ps), the DPD-n $C^S(t)$ correlations resemble those from the slower DPD-nn model while at longer time they follow the DPD-eff correlations.

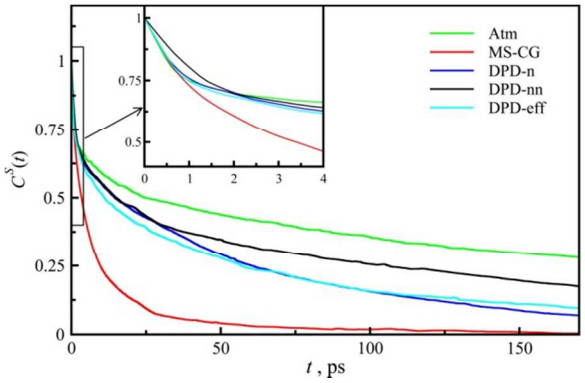

Fig. 4 Survival time correlation function, $C^S(t)$, [eqn (21)] from atomistic (green), MS-CG (red), DPD-n (blue), DPD-nn (black), and DPD-eff (cyan) simulations of liquid RDX. Insets enlarge the countered regions as indicated by arrows.

Since the DPD-n and DPD-nn models share the same frictions between nearest neighbors [which are dominated by the $\gamma^{\perp}(R)$] and at the same time the DPD-n model (for which the radial

dissipation is insignificant) demonstrates a much improved short-time behavior, we may conclude that the shear dissipation plays a dominant role in developing the distinct short-time dynamics in liquid RDX. These observations gain further support from a comparison of the liquid and crystal VDOS discussed in detail in the ESI. In particular, the DPD-n model produces the most accurately shaped VDOS while the DPD-nn,-eff have their vibrational spectra shifted toward low frequencies indicating a deteriorated short-time behavior. Furthermore, the DPD-n model yields a surprisingly improved VDOS for the crystal. The crystal dynamics is essentially caged dynamics and hence the fact that it is well represented by the DPD-n model further suggests the importance of shear dissipation to capture such dynamics accurately. For RDX, it points to the dominance of the $\gamma^{\perp}$ across different phases, and not limited to the liquid phase.

The next important transport property we evaluated is the shear viscosity, which has proved difficult to fine tune simultaneously with diffusion in conventional DPD without introducing shear dissipative forces.[42] In the past the viscosity of liquid HMX, which is chemically related to RDX, has been determined from MD simulations with the SB force field using the algorithm based on the GK relation.[63] The simulated $c_{\sigma\sigma}^{xy}(t)$ correlation function and corresponding $\eta(t)$ derived using GK relation in eqn (19) for different models on various time scales are displayed in Fig. 5; converged values $\eta = \eta(t \to \infty)$ are compiled in Table 1. On short times, the atomistic $c_{\sigma\sigma}^{xy}(t)$ exhibits a well behaved structure reflecting the fast relaxation of the stress component associated with the intramolecular bonds (Fig. 5a). However, for atomistically simulated molecular liquids the time needed for the $\eta(t)$ to converge is determined by much slower rotational and translational dynamics and typically is on the order of hundreds of picoseconds.[63-64] In the frictionless MS-CG simulation the shear viscosity converges after about 4-6 ps (Fig.

5b). For the DPD models, the dissipative forces slow down the molecular diffusion increasing the time for the $\eta(t)$ to converge, e.g., to about 200 ps for slowest DPD-nn model (Fig. 5c) which is fairly similar to the convergence time for the atomistically simulated $\eta(t)$. The time scale on which the DPD $\eta(t)$ functions evolve is determined solely by the conservative and friction forces, while the stochastic forces do not contribute much to its long-time evolution, as shown in a comparison of the $\eta(t)$ in which stochastic force contributions were included or omitted (the blue no-symbol and circle curves, respectively, in Fig. 5b). All DPD models yielded very similar values for shear viscosity (Table 1), and can be regarded as equal within the standard errors of the method. However, similar to diffusion constants, these values are significantly lower than the atomistic viscosity. The similarity in shear viscosity properties across MS-CG/DPD models could be explained by a very weak dependency of the shear viscosity on the $\gamma^{\parallel}(R)$ (it does not influence the viscosity in linear order).[42] In contrast, the η is controlled mostly by the $\gamma^{\perp}(R)$ which remains similar across the models, i.e., the averaged friction $\overline{\gamma}^{\perp}$ for the models vary to within 2% (see Table 1).

The shear viscosity is a measure of system response to shear stresses and develops primarily due to two mechanism: momentum transport and cohesive forces between the molecules. In a dense molecular liquid composed of bulky low symmetry molecules like molten RDX, the viscosity forces are due more to overcoming the cohesive intermolecular forces (which are a manifestation of caging effects discussed above) than momentum transport carried by molecules (since molecular diffusion is low). The comparative analysis of residential times, correlation functions, and viscosity by the different DPD models presented here indicates that the accurate shear frictions significantly improve the ability of the DPD to model such cohesive forces by

making the short-time dynamics to be more realistic. Therefore, the bottom-up representation of the shear friction could be of great significance for the CG simulations of macromolecular and biological systems, especially those carried out at high resolution coarse-graining.[3, 65]

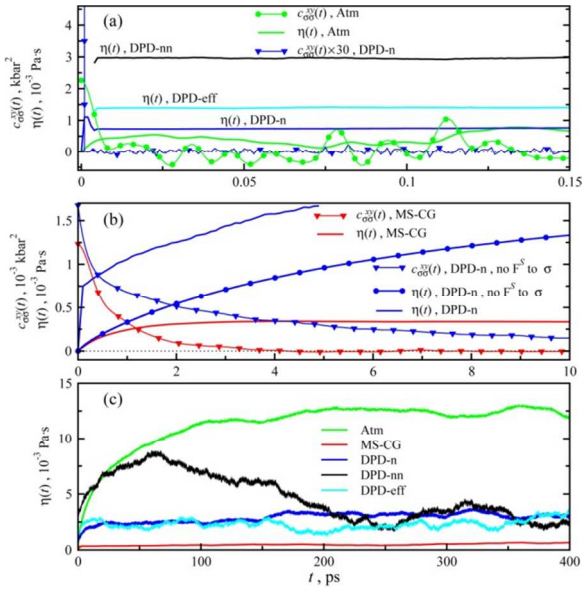

Fig. 5 The stress autocorrelation function $c_{\sigma\sigma}^{xy}(t)$ and running average viscosity $\eta(t)$ [eqn (19)] from various simulations. In all panels, the lines without symbols display the $\eta(t)$: MS-CG (red), DPD-n (blue), DPD-nn (black), and DPD-eff (cyan). Panel (a): The short-time portion of the $c_{\sigma\sigma}^{xy}(t)$ and $\eta(t)$. The atomistic $c_{\sigma\sigma}^{xy}(t)$ is shown in green line and circles, and the DPD-n $c_{\sigma\sigma}^{xy}(t)$, which is scaled by a factor of thirty for clarity, is shown in blue line and triangles. Panel (b): Comparison of MS-CG $c_{\sigma\sigma}^{xy}(t)$ (red) and DPD-n (blue) models. For the DPD-n model the $c_{\sigma\sigma}^{xy}(t)$ (blue/triangles) and $\eta(t)$ (blue/circles) calculated without contributions from stochastic forces $\mathbf{F}_I^S$ are compared to the MS-CG $c_{\sigma\sigma}^{xy}(t)$ (red/triangles) and $\eta(t)$ (red/no symbols) calculated with contributions from all interactions. Panel (c): Long time convergence of $\eta(t)$.

The shear dissipative forces are non-central forces that lead to non-conservation of the angular momentum. This may lead to quantitatively and even qualitatively incorrect results in simulations of macroscopically inhomogeneous systems with significant shear stresses, e.g., at the contact of interfaces of fluids with different viscosities, or finite-sized objects rotating in a fluid.[41, 66] In homogeneous solutions, it may impact the stability of flow on a long time scale due an incorrect representation of momentum transport. The extensions of DPD and related SPH methods toward angular momentum conserving schemes have attracted considerable attention in the literature recently.[37, 40] These extensions can be built upon using the bottom-up approach discussed here.

For liquid NM, the present approach produced very good agreement in the diffusion and shear viscosity for the one-site representation,[47] although the coarser DPD models predicted lower diffusion and higher viscosity due to a spurious dissipation caused by the coarse-graining via Voronoi tessellation at periodic intervals. Slow diffusion and high viscosity have been reported in the past for the Markovian DPD derived within the so-called *Q*-approximation,[67] $\mathbf{F}_I^S \approx \Delta\mathbf{F}_I$, to construct friction matrixes.[43, 46] Inclusion of non-Markovian memory effects[68] to the DPD substantially improves the diffusion and viscosity in dense liquids even at aggressive coarse-granting. This might be explained by strongly coupled slow dynamics of translational (CG) and irrelevant coordinates which leads to a complex dependence of the frictions on time and particle velocities.[28-29] A similar conclusion might hold for RDX, in which the molecular rotational and conformational dynamics are strongly coupled to translational motions.[69] Furthermore, within our approach significant many-body contributions to conservative forces are not captured leading to stronger frictions [eqn (16) and discussion herein]. Hence, the observed accelerated transport

properties of the reported DPD models are indeed most likely attributed to the imposed Markovian dissipation.

4. Conclusions

We have presented fully bottom-up DPD models of a real molecular liquid (molten RDX at $T = 550$ K) with conservative and non-conservative interactions systematically derived solely from force, velocity, and coordinate data along microscopic MD trajectories. In the CG representation, the RDX molecule is mapped onto a single spherically symmetrical site that constitutes high-resolution coarse-graining by DPD standards. The conservative component of the DPD interactions was obtained via force-matching in function-free form as introduced in the MS-CG approach which is consistent with the recently derived link between coarse-grained and microscopic dynamics. The method recently proposed by us for systematic coarse-graining of dissipative forces using information on the microscopic force and velocity correlations was applied to tabulate the DPD radial $\gamma^{\parallel}(R)$ and shear $\gamma^{\perp}(R)$ friction coefficients, both indicative of the strength of the respective CG dissipative interactions. In contrast to other bottom-up DPD models of real liquids discussed in the literature, the dissipative dynamics of molten RDX appears to be dominated by the $\gamma^{\perp}(R)$. The analysis of MS-CG/DPD simulations further highlights the importance of the shear friction on the short-time dynamics and transport properties in molten RDX. Evidently, the way in which the dissipation in molten RDX is partitioned (with the shear component being dominant) is a result of concerted translational and intramolecular conformational dynamics of the low symmetry RDX molecules. This observation echoes the results from a similar MS-CG/DPD model for liquid nitromethane reported recently by us in which the radial friction dominates. The study presented here suggests that the accurate

parameterization of shear frictions by applying the bottom-up techniques is an essential ingredient in obtaining the reliable DPD simulations of soft-matter systems at high resolution coarse-graining.

Finally, our objective is a development from first principles, in which we rely only on information about the microscopic interactions from atomistic simulations, of a transferrable particle-based CG model of RDX which is able to predict both equilibrium and transport properties. The application presented in this work also demonstrates that combining the bottom-up MS-CG method for constructing the conservative part of the CG model with the conceptually similar method for constructing the non-conservative interactions in a function-free form opens up the possibility of obtaining DPD models of complex molecular condensed-matter systems fully from microscopic information. As such, these models are a thermodynamically most optimal pairwise and Markovian approximation of the underlying atomistic dynamics. Hence, further improvement of the predictive abilities of the models can be achieved by extending them to include memory and many-body effects; this will be pursued in the future.

Acknowledgements

The authors wish to thank Dr. John Brennan and Dr. Joshua Moore of the Army Research Laboratory for helpful comments. This work was supported by the DoD High Performance Computing Modernization Program Software Application Institute for Multiscale Reactive Modeling of Insensitive Munitions.

Notes and references

* Weapons and Materials Research Directorate, U.S. Army Research Laboratory, Aberdeen Proving Ground, Maryland 21005, USA; *E-mail: sergiy.izvyekov.civ@mail.m*il

† Electronic Supplementary Information (ESI) available: [details of any supplementary information available should be included here]. See DOI: 10.1039/b000000x/

1. J. J. Monaghan, *Annu. Rev. Astron. Astrophys*, 1992, **30**, 543-574.
2. F. Müller-Plathe, *ChemPhysChem*, 2002, **3**, 754-769.
3. V. Tozzini, *Curr. Opin. Struct. Biol.*, 2005, **15**, 144-150.
4. C. Peter and K. Kremer, *Soft Matter*, 2009, **5**, 4357-4366.
5. W. G. Noid, *J. Chem. Phys.*, 2013, **139**, 090901.
6. P. J. Hoogerbrugge and J. M. V. A. Koelman, *Europhys. Lett.*, 1992, **19**, 155.
7. P. Español and P. Warren, *Europhys. Lett.*, 1995, **30**, 191.
8. R. D. Groot and P. B. Warren, *J. Chem. Phys.*, 1997, **107**, 4423-4435.
9. J. B. Avalos and A. D. Mackie, *Europhys. Lett.*, 1997, **40**, 141.
10. E. G. Flekkøy and P. V. Coveney, *Phys. Rev. Lett.*, 1999, **83**, 1775-1778.
11. E. G. Flekkøy, P. V. Coveney and G. De Fabritiis, *Phys. Rev. E*, 2000, **62**, 2140-2157.
12. I. Pagonabarraga, M. H. J. Hagen and D. Frenkel, *Europhys. Lett.*, 1998, **42**, 377-382.
13. R. D. Groot, *J. Chem. Phys.*, 2003, **118**, 11265-11277.
14. N. A. Spenley, *Europhys. Lett.*, 2000, **49**, 534.
15. R. D. Groot and K. L. Rabone, *Biophys. J.*, 2001, **81**, 725-736.
16. A. Vishnyakov, D. S. Talaga and A. V. Neimark, *J. Phys. Chem. Lett.*, 2012, **3**, 3081-3087.
17. L. Rekvig, M. Kranenburg, J. Vreede, B. Hafskjold and B. Smit, *Langmuir*, 2003, **19**, 8195-8205.
18. A. Ghoufi and P. Malfreyt, *Phys. Rev. E*, 2010, **82**, 016706.
19. E. S. Boek, P. V. Coveney, H. N. W. Lekkerkerker and P. van der Schoot, *Phys. Rev. E*, 1997, **55**, 3124-3133.

20. D. Kauzlaric, J. T. Meier, P. Espanol, S. Succi, A. Greiner and J. G. Korvink, *J. Chem. Phys.*, 2011, **134**, 064106.

21. H. Mori, *Prog. Theor. Phys.*, 1965, **33**, 423-455.

22. R. Zwanzig, *J. Chem. Phys.*, 1960, **33**, 1338-1341.

23. R. Zwanzig and M. Bixon, *Phys. Rev. A*, 1970, **2**, 2005-2012.

24. R. Zwanzig, *Nonequilibrium Statistical Mechanics* Oxford University Press, New York, 2004.

25. T. Kinjo and S.-a. Hyodo, *Phys. Rev. E*, 2007, **75**, 051109.

26. A. Eriksson, M. N. Jacobi, J. Nystrom and K. Tunstrom, *J. Phys.-Condes. Matter*, 2009, **21**, 095401.

27. E. Darve, J. Solomon and A. Kia, *Proc. Natl. Acad. Sci. USA*, 2009, **106**, 10884-10889.

28. C. Hijón, P. Espanol, E. Vanden-Eijnden and R. Delgado-Buscalioni, *Faraday Discuss.*, 2010, **144**, 301-322.

29. S. Izvekov, *J. Chem. Phys.*, 2013, **138**, 134106-134116.

30. C. Hijon, M. Serrano and P. Espanol, *J. Chem. Phys.*, 2006, **125**, 204101-204108.

31. W. Schommers, *Phys. Lett. A*, 1973, **43**, 157-158.

32. A. P. Lyubartsev and A. Laaksonen, *Phys. Rev. E*, 1995, **52**, 3730-3737.

33. S. Izvekov and G. A. Voth, *J. Chem. Phys.*, 2005, **123**, 134105-134117.

34. S. Izvekov and G. A. Voth, *J. Phys. Chem. B*, 2005, **109**, 2469-2473.

35. M. S. Shell, *J. Chem. Phys.*, 2008, **129**, 144108-144107.

36. S. Izvekov, *J. Chem. Phys.*, 2011, **134**, 034104.

37. P. Español, *Europhys. Lett.*, 1997, **39**, 605.

38. P. Español, *Phys. Rev. E*, 1998, **57**, 2930-2948.

39. P. Español and M. Revenga, *Phys. Rev. E*, 2003, **67**, 026705.

40. X. Y. Hu and N. A. Adams, *Phys. Fluids*, 2006, **18**, 101702.

41. W. Pan, I. V. Pivkin and G. E. Karniadakis, *Europhys. Lett.*, 2008, **84**, 10012.

42. C. Junghans, M. Praprotnik and K. Kremer, *Soft Matter*, 2008, **4**, 156-161.

43. H. Lei, B. Caswell and G. E. Karniadakis, *Phys. Rev. E*, 2010, **81**, 026704.

44. R. L. C. Akkermans and W. J. Briels, *J. Chem. Phys.*, 2000, **113**, 6409-6422.

45. A. Eriksson, M. N. Jacobi, J. Nystrom and K. Tunstrom, *J. Chem. Phys.*, 2009, **130**, 164509-164506.

46. L. Gao and W. Fang, *J. Chem. Phys.*, 2011, **135**, 184101-184107.

47. S. Izvekov and B. M. Rice, *J. Chem. Phys.*, 2014, **140**, 104104

48. P. G. Hall, *Transactions of the Faraday Society*, 1971, **67**, 556-562.

49. S. Izvekov, M. Parrinello, C. J. Burnham and G. A. Voth, *J. Chem. Phys.*, 2004, **120**, 10896-10913.

50. S. Izvekov, P. W. Chung and B. M. Rice, *J. Chem. Phys.*, 2010, **133**, 064109.

51. S. Izvekov, P. W. Chung and B. M. Rice, *J. Chem. Phys.*, 2011, **135**, 044112.

52. S. Iuchi, S. Izvekov and G. A. Voth, *J. Chem. Phys.*, 2007, **126**, 124505.

53. W. G. Noid, J. W. Chu, G. S. Ayton, V. Krishna, S. Izvekov, G. A. Voth, A. Das and H. C. Andersen, *J. Chem. Phys.*, 2008, **128**, 244114.

54. W. G. Noid, P. Liu, Y. Wang, J. W. Chu, G. S. Ayton, S. Izvekov, H. C. Andersen and G. A. Voth, *J. Chem. Phys.*, 2008, **128**, 244115.

55. L. Y. Lu, S. Izvekov, A. Das, H. C. Andersen and G. A. Voth, *J. Chem. Theory Comput.*, 2010, **6**, 954-965.

56. S. Izvekov and J. M. J. Swanson, *J. Chem. Phys.*, 2011, **134**, 194109-194114.

57. S. Izvekov and B. M. Rice, *J. Chem. Phys.*, 2012, **137**, 094704-094714.

58. G. D. Smith, R. K. Bharadwaj, D. Bedrov and C. Ayyagari, *J. Phys. Chem. B*, 1999, **103**, 705-713.

59. G. D. Smith and R. K. Bharadwaj, *J. Phys. Chem. B*, 1999, **103**, 3570-3575.

60. L. Q. Zheng and D. L. Thompson, *J. Chem. Phys.*, 2006, **125**, 084505.

61. M. J. Cawkwell, T. D. Sewell, L. Q. Zheng and D. L. Thompson, *Phys. Rev. B*, 2008, **78**, 014107.

62. R. W. Impey, P. A. Madden and I. R. McDonald, *J. Phys. Chem.*, 1983, **87**, 5071-5083.

63. D. Bedrov, G. D. Smith and T. D. Sewell, *J. Chem. Phys.*, 2000, **112**, 7203-7208.

64. M. Mondello and G. S. Grest, *J. Chem. Phys.*, 1997, **106**, 9327-9336.

65. E. Moeendarbary, T. Y. Ng and M. Zangeneh, *Int. J. Appl. Mech.*, 2009, **1**, 737-763.

66. I. O. Goetze, H. Noguchi and G. Gompper, *Phys. Rev. E*, 2007, **76**, 046705.

67. T. Koide and T. Kodama, *Phys. Rev. E*, 2008, **78**, 051107.

68. Y. Yoshimoto, I. Kinefuchi, T. Mima, A. Fukushima, T. Tokumasu and S. Takagi, *Phys. Rev. E*, 2013, **88**, 043305.

69. S. G. Boyd and K. J. Boyd, *J. Chem. Phys.*, 2008, **129**, 134502